Exchange bias switching in an antiferromagnet/ferromagnet bilayer driven by spin-orbit torque

Shouzhong Peng[1,2†], Daoqian Zhu[1†], Weixiang Li[1,2], Hao Wu[3], Alexander J. Grutter[4], Dustin A. Gilbert[4,5], Jiaqi Lu[1,2], Danrong Xiong[1], Wenlong Cai[1], Padraic Shafer[6], Kang L. Wang[3] and Weisheng Zhao[1,2]*

[1]Fert Beijing Institute, Beijing Advanced Innovation Center for Big Data and Brain Computing, School of Microelectronics, Beihang University, Beijing 100191, China

[2]Hefei Innovation Research Institute, Beihang University, Hefei 230013, China

[3]Department of Electrical Engineering, University of California, Los Angeles, CA 90095, USA

[4]NIST Center for Neutron Research, National Institute of Standards and Technology, Gaithersburg, MD 20899-6102, USA

[5]Materials Science and Engineering, University of Tennessee, Knoxville, TN 37919 USA

[6]Advanced Light Source, Lawrence Berkeley National Laboratory, Berkeley, CA 94720, USA

[†]These authors contributed equally to this work

*e-mail: weisheng.zhao@buaa.edu.cn

Abstract

The electrical manipulation of magnetization and exchange bias in antiferromagnet/ferromagnet thin films could be of use in the development of the next generation of spintronic devices. Current-controlled magnetization switching can be driven by spin-orbit torques generated in an adjacent heavy metal layer, but these structures are difficult to integrate with exchange bias switching and tunnelling magnetoresistance measurements. Here, we report the current-induced switching of exchange bias field in a perpendicularly magnetized IrMn/CoFeB bilayer structure using a spin-orbit torque generated in the antiferromagnet IrMn layer. By manipulating the current direction and amplitude, independent and repeatable switching of the magnetization and exchange bias field below the blocking temperature can be achieved. The critical current density for the exchange bias switching is found to be larger than that for CoFeB magnetization reversal. X-ray magnetic circular dichroism, polarized neutron reflectometry measurements and micromagnetic simulations show that a small net magnetization within the IrMn interface plays a crucial role in these phenomena.

Electrical manipulation of the magnetization and exchange bias in antiferromagnet (AFM)/ferromagnet (FM) heterostructures[1-10] is expected to be of use in several high-performance spintronic devices, including magnetic tunnel junctions and magnetoresistance sensors. An efficient method for electrical switching of the FM magnetization is to use the spin–orbit torque (SOT) generated from a heavy metal (such as W, Ta, Pt) layer in AFM/FM/heavy metal structures[4,5,11-14]. The in-plane exchange field generated at the AFM/FM interface enables field-free switching of the perpendicular magnetization and, compared to spin-transfer torque (STT)-driven devices, SOT-driven systems can potentially offer decreased switching times and thus faster data writing[15]. However, manipulation of the exchange bias is usually achieved by field cooling, which requires an external magnetic field and high temperature, hindering its application in practical devices[1,16,17].

Alternatively, it has recently been demonstrated that the exchange bias field at the AFM/FM interface can be switched by the SOT generated in the Pt layer in a Pt/Co/IrMn structure, passing through the thin Co layer[6]. Strong SOTs can also be generated in certain AFM thin films (such as IrMn and PtMn) due to their giant spin Hall angle[18-22], allowing simpler spintronic devices to be created[23-25]. For example, field-free switching of perpendicular magnetization has been achieved in PtMn/$[Co/Ni]_n$ structures where no heavy metal layer is required, with both the in-plane exchange bias and SOT originating from the AFM/FM system[23]. An advantage of using an AFM/FM/oxide stack is that it is easier, compared to AFM/FM/heavy metal structures, to integrate tunnelling magnetoresistance (for electrical reading of FM magnetization[26,27]), SOT and exchange bias switching in a single device.

In this Article, we report the current-induced switching of the exchange bias field by the SOT generated from the AFM IrMn layer in IrMn/CoFeB/MgO heterostructures. Controlling the

orientation of the interfacial IrMn spins, and hence the exchange bias field, and the magnetization direction of the CoFeB yields four unique states in this system. The current-controlled switching between these states is demonstrated by modulation of the current direction and amplitude, and the critical current density for exchange bias switching is experimentally determined. The underlying mechanism is investigated by X-ray magnetic circular dichroism (XMCD) and polarized neutron reflectometry (PNR) measurements to directly probe the depth- and element-specific magnetization contributions of the constituent layers. Furthermore, temperature-dependent measurements and micromagnetic simulations are used to evaluate the impact of the anisotropy energy of the interfacial pinned spins on the exchange bias manipulation.

Sample preparation and magnetic properties

Thin films of Ta(2 nm)/$Ir_{20}Mn_{80}$(5 nm)/$Co_{40}Fe_{40}B_{20}$(t_{CoFeB})/MgO(2.5 nm)/Al_2O_3(5 nm) with t_{CoFeB} of 1.1 nm to 1.2 nm are deposited on thermally oxidized Si substrates by magnetron sputtering (Fig. 1a). After deposition, the samples are annealed under a strong perpendicular magnetic field (more details can be found in the Methods). Magnetization hysteresis loops measured with out-of-plane and in-plane magnetic fields are shown in Fig. 1b and Fig. 1c, respectively, with t_{CoFeB} = 1.2 nm. The samples exhibit strong perpendicular magnetic anisotropy (PMA) and an exchange bias (EB) field ($\mu_0 H_{EB}$) of 1.1 mT in the out-of-plane direction, as shown in Fig. 1b.

The films are then patterned into Hall bar devices using standard photolithography and dry etching techniques. Figure 1d shows a micrograph of the Hall bar device and illustration of the measurement setup. A current pulse with a width of 10 ms and delay of 100 ms is applied along the longitudinal (x-direction) channel while the voltage is measured along the transverse (y-direction) channel. An exchange bias field of 1.6 mT is obtained by measuring the anomalous Hall resistance

(R_{Hall}) under perpendicular magnetic fields (Fig. 1e), in accordance with the result from the magnetization hysteresis loop. The temperature dependence of the exchange bias is shown in Fig. S1 (see Section 1 in the Supplementary Information), where a clear increase in the exchange bias field can be observed when the temperature decreases. In addition, the current-induced SOTs are measured using the harmonic technique[28-30] (see Section 2 in the Supplementary Information). The spin Hall angle (θ_{SH}) for the samples with t_{CoFeB} = 1.2 nm is measured to be 0.04, which possesses the same sign as that for IrMn in previous reports[19,20], but the opposite sign to that for Ta[13], indicating that the SOT in our samples originates mainly from the IrMn layer rather than from the Ta buffer layer. Further, SOT-driven magnetization switching is achieved in the presence of an in-plane magnetic field of $\mu_0 H_{\mathrm{x}}$ = 100 mT, as shown in Fig. 1f.

SOT-driven exchange bias switching

Exchange bias switching driven by current-induced SOT is observed in the IrMn/CoFeB/MgO structures. Figure 2a illustrates four states for the CoFeB magnetization and the interfacial IrMn spins: the up-parallel ($\mathrm{U_P}$) state, down-parallel ($\mathrm{D_P}$) state, up-antiparallel ($\mathrm{U_{AP}}$) state, and down-antiparallel ($\mathrm{D_{AP}}$) state, where the up and down represent the orientation of the FM magnetization, while the parallel and antiparallel represent the relative orientation between FM magnetization and the interfacial AFM spins. The transitions among these four states are shown with black and blue arrows. By applying an out-of-plane magnetic field, the magnetization direction can be reversed, while the orientation of the interfacial AFM spins, and hence the exchange bias field, remains unchanged, leading to transitions between the $\mathrm{U_P}$ and $\mathrm{D_{AP}}$ states, as shown in Fig. 2b. Switching of the magnetization from up to down can also be realized by applying a negative pulse current in the presence of an in-plane magnetic field of $\mu_0 H_{\mathrm{x}}$ = 100 mT, as shown in Fig. 2c. Interestingly, the

exchange bias field before the magnetization switching is -1.3 mT (Fig. 2b), but it changes to 1.6 mT after the magnetization switching (Fig. 2d), indicating reversal of the exchange bias field from negative to positive driven by the SOT current. In addition, reversal of the exchange bias field from positive to negative is demonstrated in Section 3 of the Supplementary Information. Usually, the exchange bias can be modulated by field annealing, that is to simultaneously apply an external magnetic field and a temperature higher than the blocking temperature. Here, we demonstrate that the exchange bias can also be switched by a current, which is essential for practical applications.

Next, we explore the independent switching of magnetization and exchange bias field to investigate the relationship between them. We find that when a relatively small current (e.g. 7 mA) is applied to a sample with D_P state, only the magnetization switches, while the exchange bias field remains unchanged, leading to a transition from D_P to U_{AP} state, as shown in Fig. 2e. This indicates that the critical switching current for the CoFeB magnetization is smaller than that for exchange bias field, which will be discussed in detail later. Then, in-plane pulse currents with amplitude of 8 mA or -8 mA are applied to the samples with U_{AP} state. After applying positive currents, the exchange bias field is reversed alone, but the magnetization remains unswitched, resulting in a transition from U_{AP} to U_P state (see Fig. 2f-h). In contrast, after applying negative currents, the magnetization is reversed alone, but the exchange bias field remains unswitched, resulting in a transition from U_{AP} to D_P state (see section 4 of the Supplementary Information). These results show independent switching of exchange bias field and magnetization depending on the SOT current polarity.

In order to further illustrate the current polarity dependence of exchange bias switching, it is necessary to present bidirectional switching of exchange bias field depending on the polarity of SOT

currents, while the CoFeB magnetization remains unswitched. However, because the critical switching current for exchange bias field is observed to be larger than that for the CoFeB magnetization, the exchange bias switching from a parallel initial state is usually accompanied by the reversal of CoFeB magnetization (e.g. U_P to D_P state in Fig. 2b-d). Therefore, we apply an external magnetic field with a magnitude of 250 mT and an inclined angle θ of about 3° from the sample plane. This magnetic field possesses a perpendicular component to fix the CoFeB magnetization upwards and an in-plane component to assist the SOT switching. Figure 3a-d demonstrates the transition from U_P to U_{AP} state upon applying a negative SOT current in a sample with t_{CoFeB} = 1.14 nm. We can see that the CoFeB magnetization remains unswitched (see Fig. 3c) even when I = -9 mA is applied, while the exchange bias field is reversed from negative to positive (see Fig. 3b and 3d) under the effect of SOT, leading to the transition from U_P to U_{AP} state. Then a positive current (I = 9 mA) causes the switching of exchange bias field from positive to negative with CoFeB magnetization still pointing up, resulting in the transition from U_{AP} back to U_P state (see Section 5 in Supplementary Information). Moreover, the transitions between D_P and D_{AP} states depending on the SOT current polarity are demonstrated in Fig. 3e-h and Section 5 in Supplementary Information, where the perpendicular component of the external field fixes the CoFeB magnetization downwards. These results clearly show the current polarity dependence of exchange bias switching.

Besides, we note that the current passing through the metal layers will lead to a rise in temperature due to the Joule heating effect, as demonstrated in Section 6 of the Supplementary Information. However, when a pulse current of 8 mA is applied, the temperature is measured to be 367 K, which is much lower than the blocking temperature (estimated as higher than 400 K), indicating that Joule

heating is not the primary reason for the exchange bias switching.

XMCD and PNR measurements

The exchange bias effect[31,32] has long been attributed to interfacial coupling between uncompensated moments on the surface of an antiferromagnet, with the spins in a neighboring ferromagnet[33]. X-ray[34] and neutron scattering experiments[35] support this model and emphasize a distinction between pinned uncompensated moments which contribute to exchange bias, and rotatable uncompensated moments, which do not. These techniques are applied here to investigate exchange bias in the IrMn/CoFeB system.

X-ray magnetic circular dichroism is a technique which provides element-specific sensitivity to uncompensated moments. A sample was prepared by field annealing along the film normal (out-of-plane) direction to align the antiferromagnet. The Fe and Mn X-ray absorption (XA, shown in Section 7 of Supplementary Information) and XMCD were then measured with the X-rays and a 450 mT magnetic field applied at 20° grazing incidence. This field saturates the magnetization in-plane, including the CoFeB and any rotatable moments in the IrMn. The XMCD signal from the Fe, Fig. 4a, indicates its parallel alignment with the magnetic field; the Mn signal in Fig. 4b indicates a small net magnetization from the IrMn oriented antiparallel to the Fe. The alignment of the Mn antiparallel to the magnetic field incurs a Zeeman energy cost, implying the Mn and CoFeB must possess a compensating antiparallel coupling. This also suggests that the uncompensated Mn moments are located at the IrMn/CoFeB interface. The magnetic field was then reduced to 10 mT and the sample was rotated such that the X-rays and applied field were along the film normal, and the XA/XMCD spectrums were remeasured. The new spectrums indicate that the Fe and uncompensated Mn spins realign to the out-of-plane orientation while maintaining their antiparallel

configuration. Comparing the Mn XMCD signal measured with a large in-plane versus a small out-of-plane field reveals nearly the same magnitude, within approximately 5%, suggesting virtually all of the Mn has rotated to follow the CoFeB. Lastly, the field was reduced to zero and the sample was rotated back to the 20° grazing incidence geometry and the XA/XMCD was measured. The Fe spectrum shows a small signal, likely due to the projection of the out-of-plane moment due to the 20° alignment, but no detectable signal in the Mn spectrum, indicating no residual in-plane magnetization exists from the Mn. Thus, we may conclude that as much as 95% (representing the detection limit) of the uncompensated moments within the IrMn are rotatable while the rest are pinned.

Polarized neutron reflectometry allows the magnetization to be spatially resolved along the depth of the sample. For these measurements, the sample is annealed with an in-plane field. Measurements were performed with an in-plane field of 700 mT and 2 mT. The high field condition is performed to pull the CoFeB magnetization in-plane, while for the low-field measurement, the CoFeB will rotate out-of-plane due to its perpendicular anisotropy. The small field (2 mT) is necessary to maintain the polarization of the neutron beam during the measurement. Based on the XMCD data, the rotatable Mn spins in the low-field measurement are expected to follow the CoFeB magnetization out-of-plane, while any pinned Mn spins will remain in-plane. Since PNR is exclusively sensitive to in-plane magnetization, the low-field measurement will only be sensitive to the pinned Mn moments.

Figure 4c shows the PNR data and modeled curves as a function of the perpendicular momentum transfer vector Q (the spin asymmetry is shown in Section 8 of the Supplementary Information). The theoretical curves are consistent with the experimental results, capturing all of the major

features. The converged model of the sample's depth-resolved scattering length density (SLD), used to calculate the theoretical curves in Fig. 4c, is shown in Fig. 4d. For both of the field conditions, only a small antiparallel magnetization may be present at the IrMn interface (red line in Fig. 4d), consistent with the small Mn XMCD signal. The best fit to the data includes a magnetization of 45 ± 12 $KA \cdot m^{-1}$ in the 700 mT measurement and 10 ± 8 $KA \cdot m^{-1}$ in 2 mT, which oriented antiparallel to the CoFeB and the magnetic field. The magnetization in the 2 mT measurement is much smaller than that in the 700 mT measurement, suggesting that the pinned Mn spins are a small minority of the uncompensated spins. Using these magnetization values, the PNR is consistent with a picture in which approximately 9% of the Mn at the interface is uncompensated, and of that 95% is rotatable and follows the CoFeB. It is important to acknowledge here that such small interfacial moments are difficult to demonstrate conclusively through PNR in this system due to the proximity of the large CoFeB moment. Rather, the PNR specifically indicates that models which incorporate an overall IrMn moment favor antiparallel alignment and show no evidence that the majority of such a moment is strongly pinned rather than rotating to remain antiparallel with the CoFeB. Thus, the XMCD and PNR results are in agreement, indicating a majority of the uncompensated Mn moments, which are located at the IrMn surface, are rotatable and align anti-parallel to the CoFeB.

Micromagnetic simulations of exchange bias switching

Based on these observations, micromagnetic simulations (see the Methods) are performed to explore the existence of exchange bias and its manipulation by SOT in our experiments. Figure 5a shows the schematic of the AFM/FM exchange bias system, including the bulk AFM, the interfacial AFM spins and the FM layer. The interface consists of two types of uncompensated spins[34-36], i.e., the pinned spins which, marked in red, remain nearly unchanged under the stimulus of external

magnetic fields and the rotatable spins which, marked in blue, can switch with the FM magnetization. Based on the XMCD and PNR results, only a small number of interfacial spins are set as pinned spins (see Section 9 in the Supplementary Information) while others are rotatable. Perpendicular magnetic fields are swept before and after a SOT pulse to obtain the corresponding exchange bias field.

Initially, a positive exchange bias field is obtained, as shown in Fig. 5b. When we apply a SOT current of J_{SOT} = 90 MA·cm^{-2}, the FM magnetization can be switched (not shown) while the exchange bias field is still positive, as indicated in Fig. 5c. Moreover, Fig. 5c also shows that a large SOT current (J_{SOT} = 270 MA·cm^{-2}) can be used to reverse the exchange bias field, which implies that the switching current density for exchange bias field is larger than that for FM magnetization. This is ascribed to the large anisotropy difference between the pinned spins and the FM magnetization in our simulations and is further verified in the temperature-dependent experiments (see the next section). Figure 5d and 5e are snapshots of the z component of FM magnetization at selected times upon the application of different SOT currents. Due to the Heisenberg interaction, the FM magnetization marked by the black dashed circles are consistent with the interfacial pinned spins beneath the FM layer. When J_{SOT} = 90 MA·cm^{-2} is applied, a domain wall (DW) nucleates at the edge and then propagates through the sample. However, the anisotropy difference between the pinned spins and FM magnetization induces a strong pinning force, thus the domain expansion stops at the pinned area. With the FM magnetization almost switched, the pinned spins remain unchanged (see the marked areas), still generating a positive exchange bias field. In contrast, the DW can be gradually depinned when a large SOT current (J_{SOT} = 270 MA·cm^{-2}) is applied, as shown in Fig. 5e. Therefore, the pinned spins are finally switched, resulting in a negative exchange bias field.

Through sweeping the SOT current density, it is clearly shown in Fig. 5f that the critical switching current density for the exchange bias is larger than that for the magnetization. Based on this phenomenon, the FM magnetization and exchange bias can be independently manipulated using different SOT currents rather than via perpendicular magnetic fields (see Section 10 in the Supplementary Information). Both our simulation and experimental results illustrate that the physical mechanism of SOT-driven exchange bias switching would be related to the switching of pinned spins at the AFM/FM interface. The switching behaviour of interfacial pinned spins driven by SOT current is similar to that of FM magnetization, but the pinned spins possess stronger magnetic anisotropy, leading to larger critical switching current for the exchange bias. However, the impact of the bulk property of AFM on the exchange bias switching have not been identified in our study. Further investigation on AFM/FM bilayer system requires direct detection of magnetic moments in the bulk AFM.

Temperature- and thickness-dependent switching

To confirm the different critical current densities for magnetization and exchange bias field, temperature- and thickness-dependent switching are explored. Figure 6 demonstrates reversal of magnetization and exchange bias field driven by gradually increasing currents. The Hall resistance (left axis) and the exchange bias field (right axis) are measured after each current is applied. For the samples with CoFeB thickness t_{CoFeB} = 1.2 nm and temperature T = 300 K (see Fig. 6a), sharp magnetization switching occurs at a current of 6 mA (corresponding to 12.7 MA·cm^{-2}), while the exchange bias field remains almost unchanged, making switching of the magnetization alone possible. By gradually increasing the pulse current, exchange bias switching occurs at a current of 8 mA, showing an obviously larger critical switching current for the exchange bias field than for the

FM magnetization. Furthermore, two methods are demonstrated to modulate the critical switching current for the exchange bias field. The first method is controlling the thickness of the FM layer. As shown in Fig. 6c, for the samples with thinner CoFeB layers (t_{CoFeB} = 1.1 nm), a larger critical current (>10 mA) is required to achieve switching of the exchange bias field. The second method is adjusting the temperature. By decreasing the temperature to 255 K, the critical switching current increases, as shown in Fig. 6b; while the critical current decreases when increasing the temperature to 345 K, resulting in exchange bias switching for the samples with t_{CoFeB} = 1.1 nm, as shown in Fig. 6d. More details about temperature dependence of exchange bias switching can be found in Section 11 of the Supplementary Information. These results demonstrate effective manipulation of magnetization and exchange bias through control of temperature and CoFeB thickness.

Conclusion

We have reported current-induced exchange bias switching via the SOT originating from the AFM layer in an IrMn/CoFeB bilayer. The independent switching of magnetization and exchange bias field in a repeatable manner is demonstrated by manipulating the current direction and amplitude in the presence of an in-plane magnetic field. Experimental results from PNR and XMCD indicate a small net magnetization exists at the IrMn interface, comprised primarily of rotatable uncompensated Mn spins and a much smaller fraction (<10%) of pinned spins. Micromagnetic simulations and temperature-dependent measurements show that the critical current density to switch the interfacial pinned spins, and hence the exchange bias field, is larger than that of magnetization reversal, and this difference allows the FM layer and exchange bias to be individually manipulated by SOT currents, rather than via perpendicular magnetic fields.

Methods

Ultrahigh-vacuum magnetron sputtering was used to deposit sub./Ta(2 nm)/$Ir_{20}Mn_{80}$(5 nm)/$Co_{40}Fe_{40}B_{20}$(t_{CoFeB})/MgO(2.5 nm)/Al_2O_3(5 nm) stacks without applying an external magnetic field during deposition. The CoFeB thickness (t_{CoFeB}) is 1.1 nm to 1.2 nm. Ta was used as the buffer layer. After deposition, the samples were annealed in vacuum (<10^{-7} Torr) at 200°C for 30 minutes under a perpendicular magnetic field of 1.5 T. The magnetic properties of the blank stacks were studied with a vibrating sample magnetometer. Subsequently, standard photolithography and dry etching techniques were utilized to pattern the thin films into Hall bar devices. The widths of the longitudinal channel and the transverse channel for the Hall bar devices were 5 μm and 3 μm, respectively.

X-ray absorption (XA) and X-ray magnetic circular dichroism (XMCD) were performed at beamline 4.0.2 of the Advanced Light Source. Sample stacks were composed of Ta(5 nm)/$Ir_{20}Mn_{80}$(5 nm)/$Co_{40}Fe_{40}B_{20}$(1 nm)/MgO(2 nm)/Ta(2 nm). Measurements were performed with the applied field along the X-ray propagation direction. Since the objective of the XMCD study was to determine the fraction of uncompensated IrMn spins which follow the CoFeB, in the inherently uniaxial exchange biased state, it was important to perform the XMCD measurements with alternating photon helicity rather than alternating applied field. Further, alternating field is not possible when studying the final in-plane remnant state. All measurements were therefore performed using alternating photon helicity with ±0.9 circular polarization. The data was collected at room temperature in total electron yield mode. The sample was aligned either with the applied magnetic field and X-ray propagation direction along the film normal or along in grazing incidence with the beam and field inclined at 20° relative to the film plane.

Polarized neutron reflectometry (PNR) was performed using the PNR instrument at the NIST

center for neutron research. Incident and scattered neutrons were polarized either parallel or antiparallel to the applied field direction. Because of the perpendicular anisotropy of the CoFeB, only net magnetization contributions are expected parallel to the applied field or along the out-of-plane direction. No spin-flip scattering is therefore expected, and measured only the non-spin-flip cross sections. We therefore collected the ↑↑ and ↓↓ scattering cross sections as a function of the perpendicular momentum transfer vector Q. Data was reduced using the reductus software program and fit with the Refl1D software package[37,38].

Micromagnetic simulations were performed using the GPU-accelerated platform Mumax3[39]. In our simulations, the pinned spins possess a higher effective anisotropy than the rotatable spins[40] whose anisotropy strength equals to that of the FM layer. According to the XMCD and PNR results, antiparallel coupling is set between the rotatable spins and the FM magnetization. Considering that the initial hysteresis of our samples is oppositely shifted to the field cooling direction, even under a magnetic field of +5 T, the interfacial pinned spins are speculated to ferromagnetically couple with the FM layer[41], as set in the model. Note that in our simulations, we only consider the FM magnetization (three layers) and one layer of interfacial spins because previous studies have indicated that interfacial spin orders behave basically independently with the adjacent bulk AFM grains when modulating the exchange bias[42]. Though the influence of the bulk AFM cannot be ruled out, the main features in our experiments can be well reproduced with this simplification. Based on the previous reports on the grain size in IrMn/CoFeB[43,44], both the FM layer and interfacial AFM were divided into grains with an average size of 10 nm using a Voronoi tessellation, and the position of grains in the FM layer did not coincide with that in interfacial AFM[40]. The applied SOT pulses last for 10 ns and then are removed, relaxing the system for 10 ns. All the simulations were

performed at a temperature of 300 K except that the hysteresis was recorded at 0 K to exclude thermal effects. For material parameters adopted in our simulations, see Section 12 in the Supplementary Information.

Data availability

The data that support the plots within this paper and other findings of this study are available from the corresponding author upon reasonable request.

Code availability

The micromagnetic simulator Mumax3 used in this work is publicly accessible at https://mumax.github.io/.

References

1. Baltz, V. *et al.* Antiferromagnetic spintronics. *Rev. Mod. Phys.* **90**, 015005 (2018).
2. Jungwirth, T., Marti, X., Wadley, P. & Wunderlich, J. Antiferromagnetic spintronics. *Nat. Nanotechnol.* **11**, 231–241 (2016).
3. Wadley, P. *et al.* Electrical switching of an antiferromagnet. *Science* **351**, 587–591 (2016).
4. Lau, Y. C., Betto, D., Rode, K., Coey, J. M. D. & Stamenov, P. Spin-orbit torque switching without an external field using interlayer exchange coupling. *Nat. Nanotechnol.* **11**, 758–762 (2016).
5. Brink, A. *et al.* Field-free magnetization reversal by spin-Hall effect and exchange bias. *Nat. Commun.* **7**, 10854 (2016).
6. Lin, P. H. *et al.* Manipulating exchange bias by spin–orbit torque. *Nat. Mater.* **18**, 335–341 (2019).
7. Kimata, M. *et al.* Magnetic and magnetic inverse spin Hall effects in a non-collinear antiferromagnet. *Nature* **565**, 627–630 (2019).
8. Chen, X. *et al.* Electric field control of Néel spin–orbit torque in an antiferromagnet. *Nat. Mater.* **18**, 931-935 (2019).
9. Yan, H. *et al.* A piezoelectric, strain-controlled antiferromagnetic memory insensitive to

magnetic fields. *Nat. Nanotechnol.* **14**, 131–136 (2019).

10. Razavi, S. A. *et al.* Joule heating effect on field-free magnetization switching by spin-orbit torque in exchange-biased systems. *Phys. Rev. Appl.* **7**, 024023 (2017).
11. Miron, I. M. *et al.* Current-driven spin torque induced by the Rashba effect in a ferromagnetic metal layer. *Nat. Mater.* **9**, 230–234 (2010).
12. Miron, I. M. *et al.* Perpendicular switching of a single ferromagnetic layer induced by in-plane current injection. *Nature* **476**, 189–193 (2011).
13. Liu, L. *et al.* Spin-torque switching with the giant spin Hall effect of tantalum. *Science* **336**, 555–558 (2012).
14. Liu, L., Lee, O. J., Gudmundsen, T. J., Ralph, D. C. & Buhrman, R. A. Current-induced switching of perpendicularly magnetized magnetic layers using spin torque from the spin Hall effect. *Phys. Rev. Lett.* **109**, 096602 (2012).
15. Baumgartner, M. *et al.* Dynamics driven by spin–orbit torques. *Nat. Nanotechnol.* **12**, 980–986 (2017).
16. Zhang, W. & Krishnan, K. M. Epitaxial exchange-bias systems: From fundamentals to future spin-orbitronics. *Mater. Sci. Eng. R Reports* **105**, 1–20 (2016).
17. Schuller, I. K. Exchange bias. *J. Magn. Magn. Mater.* **192**, 203–232 (1999).
18. Zhou, J. *et al.* Large spin-orbit torque efficiency enhanced by magnetic structure of collinear antiferromagnet IrMn. *Sci. Adv.* **5**, eaau6696 (2019).
19. Zhang, W. *et al.* Giant facet-dependent spin-orbit torque and spin Hall conductivity in the triangular antiferromagnet $IrMn_3$. *Sci. Adv.* **2**, e1600759 (2016).
20. Wu, D. *et al.* Spin-orbit torques in perpendicularly magnetized $Ir_{22}Mn_{78}/Co_{20}Fe_{60}B_{20}/MgO$ multilayer. *Appl. Phys. Lett.* **109**, 222401 (2016).
21. Ou, Y., Shi, S., Ralph, D. C. & Buhrman, R. A. Strong spin Hall effect in the antiferromagnet PtMn. *Phys. Rev. B* **93**, 220405(R) (2016).
22. Zhang, W. *et al.* Spin Hall effects in metallic antiferromagnets. *Phys. Rev. Lett.* **113**, 196602 (2014).
23. Fukami, S., Zhang, C., DuttaGupta, S., Kurenkov, A. & Ohno, H. Magnetization switching by spin–orbit torque in an antiferromagnet–ferromagnet bilayer system. *Nat. Mater.* **15**, 535–541

(2016).

24. Oh, Y.-W. *et al.* Field-free switching of perpendicular magnetization through spin–orbit torque in antiferromagnet/ferromagnet/oxide structures. *Nat. Nanotechnol.* **11**, 878–884 (2016).
25. Reichlová, H. *et al.* Current-induced torques in structures with ultrathin IrMn antiferromagnets. *Phys. Rev. B* **92**, 165424 (2015).
26. Parkin, S. S. P. *et al.* Giant tunnelling magnetoresistance at room temperature with MgO (100) tunnel barriers. *Nat. Mater.* **3**, 862 (2004).
27. Yuasa, S., Nagahama, T., Fukushima, A., Suzuki, Y. & Ando, K. Giant room-temperature magnetoresistance in single-crystal Fe/MgO/Fe magnetic tunnel junctions. *Nat. Mater.* **3**, 868–871 (2004).
28. Pi, U. H. *et al*. Tilting of the spin orientation induced by Rashba effect in ferromagnetic metal layer. *Appl. Phys. Lett.* **97**, 162507 (2010).
29. Kim, J. *et al.* Layer thickness dependence of the current-induced effective field vector in Ta|CoFeB|MgO. *Nat. Mater.* **12**, 240 (2013).
30. Khvalkovskiy, A. V. *et al.* Matching domain-wall configuration and spin-orbit torques for efficient domain-wall motion. *Phys. Rev. B* **87**, 020402 (2013).
31. Noguésa, J. *et al.* Exchange bias in nanostructures. *Phys. Rep.* **422,** 65–117 (2005).
32. Stamps, R. L., Mechanisms for exchange bias. *J. Phys. D: Appl. Phys*. **33**, 247268 (2000).
33. Meiklejohn, W. H. & Bean, C. P. New magnetic anisotropy. *Phys. Rev.* **105,** 3 (1957).
34. Ohldag, H. *et al.* Correlation between Exchange Bias and Pinned Interfacial Spins. *Phys. Rev. Lett.* **91,** 1 (2003).
35. Fitzsimmons, M. R. *et al*. Pinned magnetization in the antiferromagnet and ferromagnet of an exchange bias system. *Phys. Rev. B* **75**, 214412 (2007).
36. Dubowika, J. & Goscianska, I. Micromagnetic Approach to Exchange Bias. *Acta Phys. Polonica A.* **127,** 2 (2015).
37. Maranville, B., Ratcliff, W. & Kienzle, P. reductus: a stateless Python data reduction service with a browser front end. *J. Appl. Cryst.* **51**, 1500–1506 (2018).
38. Kirby, B. J. *et al.* Phase-sensitive specular neutron reflectometry for imaging the nanometer scale composition depth profile of thin-film materials. *Curr. Opin. Colloid In.* **17**, 44–53 (2012).

39. Vansteenkiste, A. *et al.* The design and verification of MuMax3. *AIP Adv.* **4,** 107133 (2014).

40. Clercq, J. D., Vansteenkiste, A., Abes, M., Temst, K. & Waeyenberge, B. V. Modelling exchange bias with MuMax^3. *J. Phys. D: Appl. Phys.* **49,** 435001 (2016).

41. Leighton, C., Nogués, J., Åkerman, B. J. J. & Schuller, I. K. Coercivity enhancement in exchange biased system driven by interfacial magnetic. *Phys. Rev. Lett.* **84,** 3467 (2000).

42. Grady, K., Outon, L. E. F. & Fernandez, G. V. A new paradigm for exchange bias in polycrystalline. *J. Magn. Magn. Mater.* **322**, 883–899 (2010).

43. Aley, N. P. *et al*. Texture effects in IrMn/CoFe exchange bias systems. *IEEE Trans. Magn.* **44**, 2820-2823 (2008).

44. Rajua, M., Chaudhary, S. & Pandya, D. K. Magnetic annealing of the ion-beam sputtered IrMn/CoFeB bilayers - positive exchange bias and coercivity behavior. *Eur. Phys. J. B* **86**, 491 (2013).

Acknowledgements

The authors thank the National Natural Science Foundation of China (Grant No. 61627813, 61571023), the International Collaboration Project B16001, the National Key Technology Program of China 2017ZX01032101, and the Beihang Hefei Innovation Research Institute Project BHKX-19-02 for their financial support of this work. This research used resources of the Advanced Light Source, a DOE Office of Science User Facility under contract No. DE-AC02-05CH11231.

Author contributions

W.Z. initialized, conceived and supervised the project. S.P. fabricated the devices. S.P., W.L., J.L., W.C. and D.X. performed the measurements. D.Z. performed the micromagnetic simulations. H.W. deposited the thin films under the supervision of K.W. A.G., D.G. and P.S. performed and analysed the X-ray spectroscopy and the neutron reflectometry. S.P., D.Z., A.G. and W.Z. wrote the manuscript. All authors discussed the results and implications.

Competing interests

The authors declare no competing financial interests

Additional information

Supplementary information is available in the online version of the paper.

Figure captions

Fig. 1 | Magnetic properties of the IrMn/CoFeB/MgO films and the Hall bars. a, Schematic of the IrMn/CoFeB/MgO stacks. **b**,**c,** Magnetization hysteresis loops under (**b**) perpendicular and (**c**) in-plane magnetic fields, with t_{CoFeB} = 1.2 nm. A perpendicular exchange bias field of 1.1 mT is obtained after annealing. **d**, Micrograph of Hall bar device and illustration of the setup for Hall bar measurements. **e**, Anomalous Hall resistance (R_{Hall}) under perpendicular magnetic fields. An exchange bias field of 1.6 mT is obtained, consistent with the result from the perpendicular magnetization hysteresis loop. **f**, SOT-driven magnetization switching in the presence of an in-plane magnetic field $\mu_0 H_x$ = 100 mT.

Fig. 2 | Exchange bias and magnetization switching driven by current-induced SOT. a, Schematic configurations of four states for the CoFeB magnetization and interfacial IrMn spins (up-parallel (U_P) state, down-parallel (D_P) state, up-antiparallel (U_{AP}) state, and down-antiparallel (D_{AP}) state), and transitions among them. **b-d**, Concurrent switching of the magnetization and exchange bias field driven by a pulse current in the presence of an in-plane magnetic field ($\mu_0 H_x$ = 100 mT). The measurements of exchange bias field before and after magnetization switching are shown in **b** and **d**, respectively, where the exchange bias switching from -1.3 mT to 1.6 mT can be observed. **e**, Independent switching of magnetization with a relatively small current (≤7 mA), the exchange bias field remains unchanged. **f-h**, Independent switching of exchange bias field with a positive current of 8 mA, the magnetization remains unchanged. The insets illustrate the initial states before currents are applied and the final states after the largest currents (7 mA or ±8 mA) are applied.

Fig. 3 | Bidirectional switching of exchange bias field depending on SOT current polarity. a, Schematic of transitions between U_P and U_{AP} states depending on SOT current polarity. **b-d**, Independent switching of exchange bias field from U_P to U_{AP} state with a negative current. An external magnetic field with a magnitude of 250 mT and an inclined angle θ of about 3° from the sample plane is applied. The measurements of exchange bias field before and after switching are shown in **b** and **d**, respectively. **e**, Schematic of transitions between D_P and D_{AP} states depending on SOT current polarity. **f-h**, Independent switching of exchange bias field from D_P to D_{AP} state with a positive current.

Fig. 4 | XMCD and PNR during switching. **a**,**b**, XMCD of the (**a**) Fe and (**b**) Mn in the IrMn/CoFeB structure. XMCD results have been offset for clarity and show the three field conditions of 450 mT 20° grazing (red), 10 mT out-of-plane (blue), and 0 mT 20° grazing (green). **c**, PNR and theoretical fit at 700 mT and 2 mT. Curves offset for clarity. **d**, Converged scattering length density (SLD) profile used to generate the fits in panel c. Note that the plotted profile does not show the entirety of the thermally grown SiO_2 or Si substrate.

Fig. 5 | Micromagnetic simulation results of exchange bias and its manipulation by SOT. **a** Schematic of the AFM/FM exchange bias system. **b**,**c**, Hysteresis loops **(b)** before and **(c)** after application of SOT currents when J_{SOT} = 90 MA·cm^{-2} and J_{SOT} = 270 MA·cm^{-2}. **d**,**e**, Snapshots of the z component of the FM magnetization configuration (m_z) at selected times when **(d)** J_{SOT} = 90 MA·cm^{-2} and **(e)** J_{SOT} = 270 MA·cm^{-2}. **f**, Switching of the exchange bias and magnetization under different SOT current densities. In the simulations above, an in-plane magnetic field $\mu_0 H_x$ = 30 mT is incorporated to realize deterministic SOT switching. The magnetization switching curve is from one single simulation, while the exchange bias switching is simulated six times. The error bars are standard deviations.

Fig. 6 | Temperature and thickness dependence of magnetization and exchange bias switching. a-

d, Switching of magnetization and exchange bias field driven by gradually increasing currents in the presence of an in-plane magnetic field of $\mu_0 H_x$ = 100 mT. Samples with (**a**,**b**) 1.2 nm CoFeB are investigated at (**a**) T = 300 K and (**b**) T = 255 K, while samples with (**c**,**d**) 1.1 nm CoFeB are measured at (**c**) T = 300 K and (**d**) T = 345 K. The Hall resistance (left axis) and the exchange bias field (right axis) are measured after each current is applied. The initial state is the down-parallel (D_P) state. The error bars are standard deviations.

Fig. 1

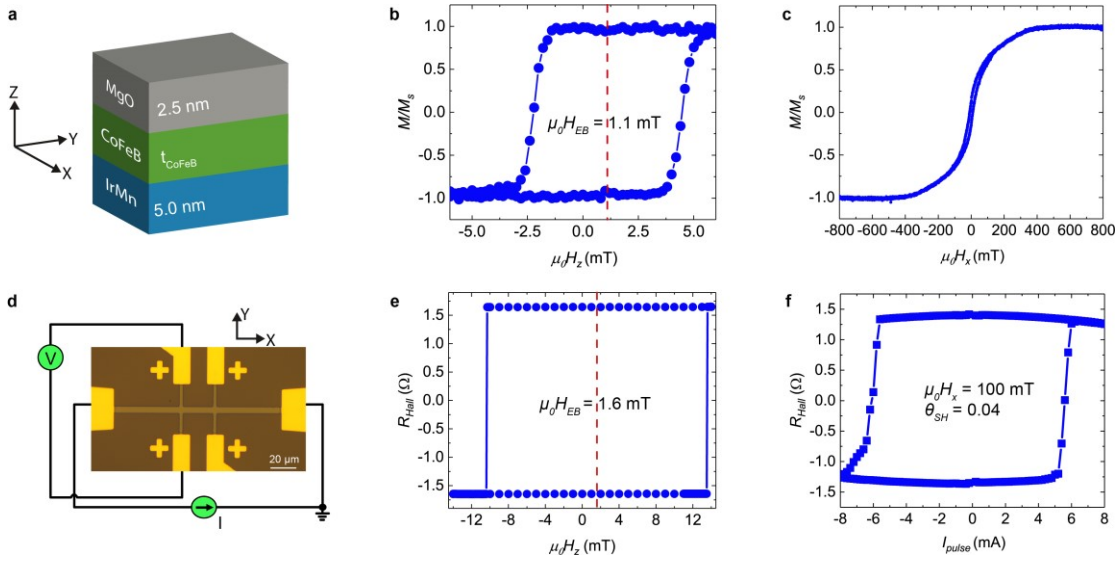
a
MgO
2.5 nm
CoFeB
t_{CoFeB}
IrMn
5.0 nm
Z
Y
X
b
M/M_s
$\mu_0 H_{EB}$ = 1.1 mT
$\mu_0 H_z$ (mT)
c
M/M_s
$\mu_0 H_x$ (mT)
d
V
Y
X
20 μm
I
e
R_{Hall} (Ω)
$\mu_0 H_{EB}$ = 1.6 mT
$\mu_0 H_z$ (mT)
f
R_{Hall} (Ω)
$\mu_0 H_x$ = 100 mT
θ_{SH} = 0.04
I_{pulse} (mA)

Fig.2

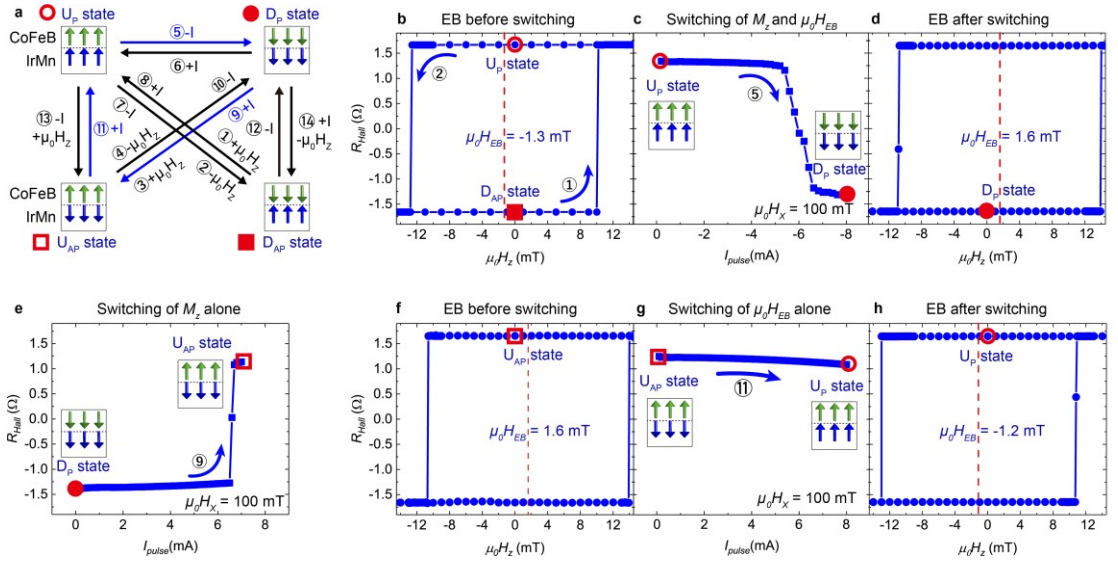
a
U_P state
D_P state
CoFeB
IrMn
⑤-I
⑥+I
⑧+I
⑩-I
⑦-I
⑨+I
⑬-I
$+\mu_0 H_z$
⑪+I
④$-\mu_0 H_z$
①$+\mu_0 H_z$
⑫-I
⑭+I
$-\mu_0 H_z$
③$+\mu_0 H_z$
②$-\mu_0 H_z$
U_{AP} state
D_{AP} state
b
EB before switching
U_P state
$\mu_0 H_{EB}$ = -1.3 mT
D_{AP} state
R_{Hall} (Ω)
$\mu_0 H_z$ (mT)
c
Switching of M_z and $\mu_0 H_{EB}$
U_P state
D_P state
$\mu_0 H_x$ = 100 mT
I_{pulse}(mA)
d
EB after switching
$\mu_0 H_{EB}$ = 1.6 mT
D_P state
$\mu_0 H_z$ (mT)
e
Switching of M_z alone
U_{AP} state
D_P state
$\mu_0 H_x$ = 100 mT
I_{pulse}(mA)
f
EB before switching
U_{AP} state
$\mu_0 H_{EB}$ = 1.6 mT
$\mu_0 H_z$ (mT)
g
Switching of $\mu_0 H_{EB}$ alone
U_{AP} state
U_P state
$\mu_0 H_x$ = 100 mT
I_{pulse}(mA)
h
EB after switching
U_P state
$\mu_0 H_{EB}$ = -1.2 mT
$\mu_0 H_z$ (mT)

Fig.3

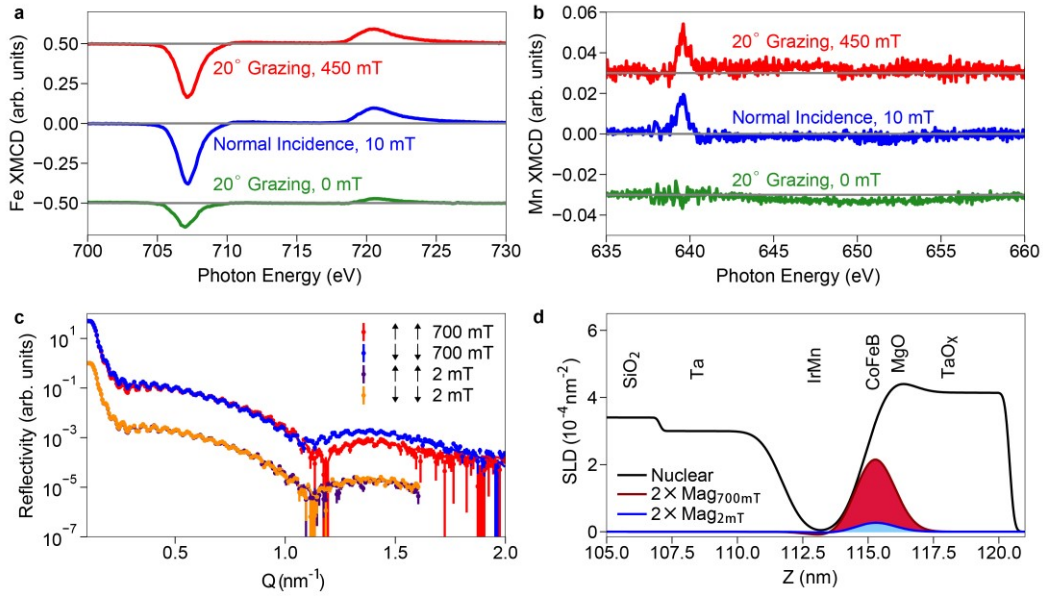
a
Fe XMCD (arb. units)
20° Grazing, 450 mT
Normal Incidence, 10 mT
20° Grazing, 0 mT
Photon Energy (eV)
b
Mn XMCD (arb. units)
20° Grazing, 450 mT
Normal Incidence, 10 mT
20° Grazing, 0 mT
Photon Energy (eV)
c
Reflectivity (arb. units)
700 mT
700 mT
2 mT
2 mT
Q (nm^{-1})
d
SLD (10^{-4}nm^{-2})
SiO$_2$
Ta
IrMn
CoFeB
MgO
TaO$_x$
Nuclear
2× Mag$_{700mT}$
2× Mag$_{2mT}$
Z (nm)

Fig.4

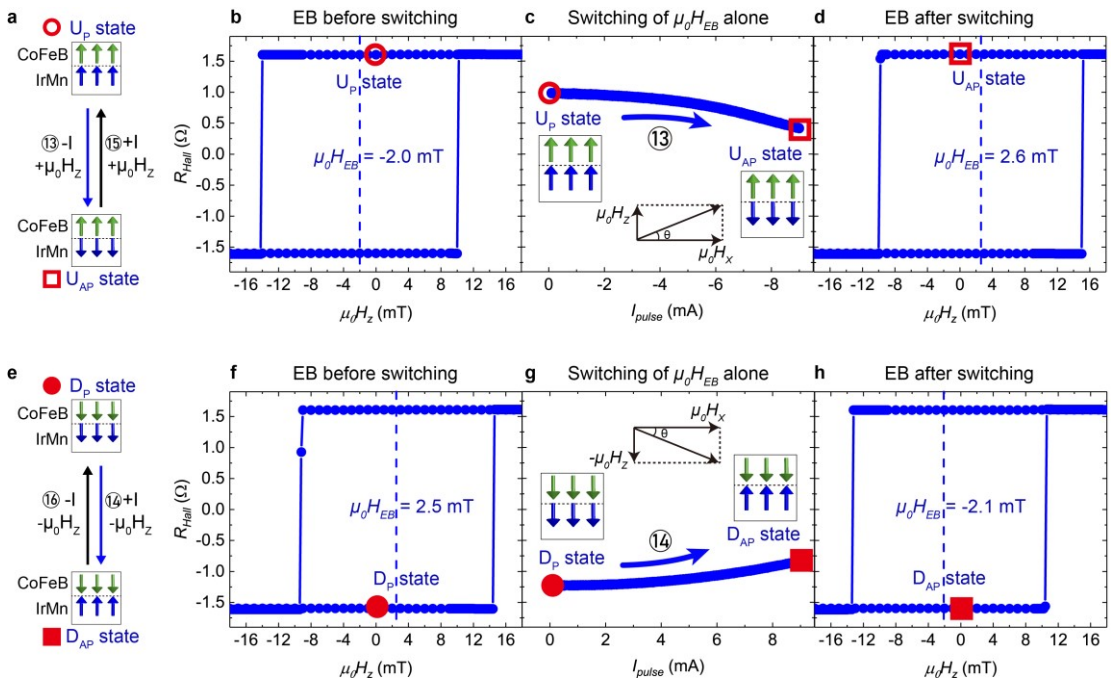
a
U$_P$ state
CoFeB
IrMn
⑬ -I
+μ$_0$H$_z$
⑮ +I
+μ$_0$H$_z$
CoFeB
IrMn
U$_{AP}$ state
b
EB before switching
U$_P$ state
μ$_0$H$_{EB}$ = -2.0 mT
R$_{Hall}$ (Ω)
μ$_0$H$_z$ (mT)
c
Switching of μ$_0$H$_{EB}$ alone
U$_P$ state
⑬
U$_{AP}$ state
μ$_0$H$_z$
θ
μ$_0$H$_x$
I$_{pulse}$ (mA)
d
EB after switching
U$_{AP}$ state
μ$_0$H$_{EB}$ = 2.6 mT
μ$_0$H$_z$ (mT)
e
D$_P$ state
CoFeB
IrMn
⑯ -I
-μ$_0$H$_z$
⑭ +I
-μ$_0$H$_z$
CoFeB
IrMn
D$_{AP}$ state
f
EB before switching
μ$_0$H$_{EB}$ = 2.5 mT
D$_P$ state
R$_{Hall}$ (Ω)
μ$_0$H$_z$ (mT)
g
Switching of μ$_0$H$_{EB}$ alone
μ$_0$H$_x$
θ
-μ$_0$H$_z$
D$_{AP}$ state
⑭
D$_P$ state
I$_{pulse}$ (mA)
h
EB after switching
μ$_0$H$_{EB}$ = -2.1 mT
D$_{AP}$ state
μ$_0$H$_z$ (mT)

Fig. 5

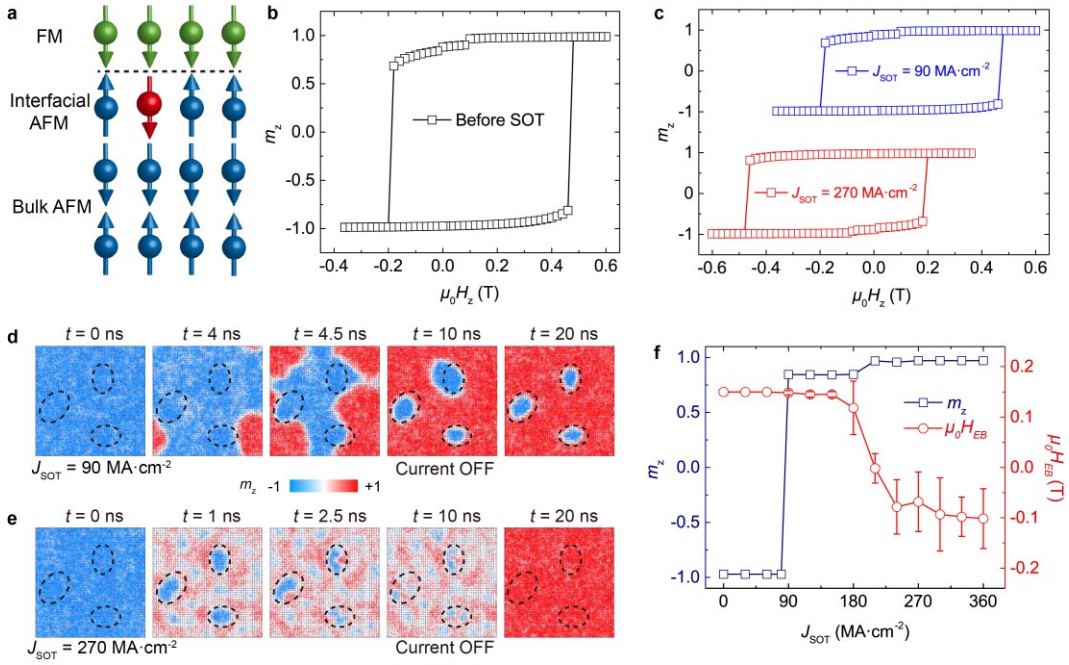
a
FM
Interfacial AFM
Bulk AFM
b
Before SOT
m_z
$\mu_0 H_z$ (T)
c
J_{SOT} = 90 MA·cm^{-2}
J_{SOT} = 270 MA·cm^{-2}
m_z
$\mu_0 H_z$ (T)
d
t = 0 ns
t = 4 ns
t = 4.5 ns
t = 10 ns
t = 20 ns
J_{SOT} = 90 MA·cm^{-2}
Current OFF
m_z -1 +1
e
t = 0 ns
t = 1 ns
t = 2.5 ns
t = 10 ns
t = 20 ns
J_{SOT} = 270 MA·cm^{-2}
Current OFF
f
m_z
$\mu_0 H_{EB}$
$\mu_0 H_{EB}$ (T)
J_{SOT} (MA·cm^{-2})

Fig.6

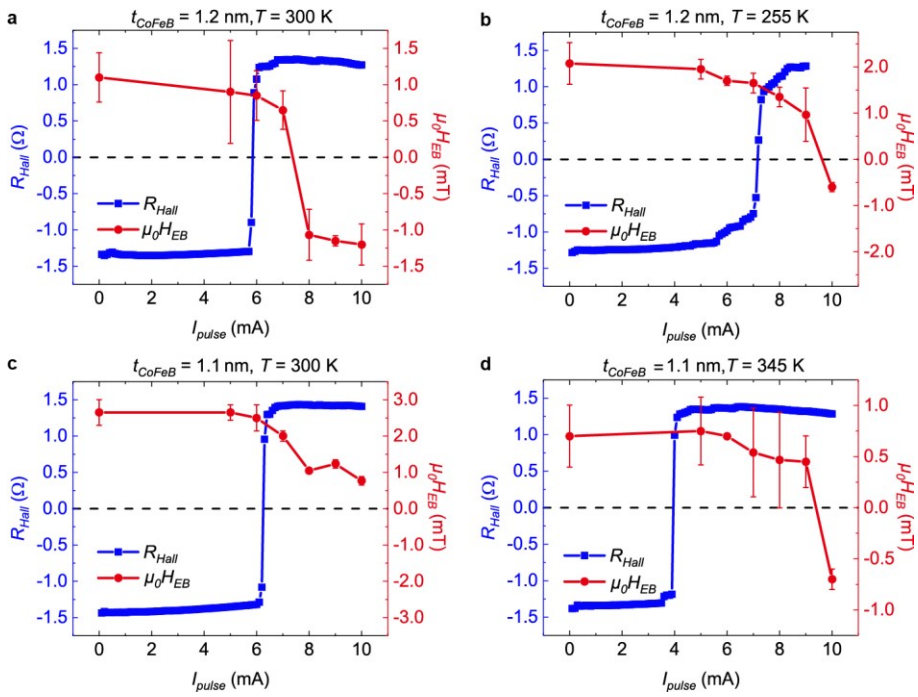
a
t_{CoFeB} = 1.2 nm, T = 300 K
b
t_{CoFeB} = 1.2 nm, T = 255 K
c
t_{CoFeB} = 1.1 nm, T = 300 K
d
t_{CoFeB} = 1.1 nm, T = 345 K
R_{Hall} (Ω)
$\mu_0 H_{EB}$ (mT)
R_{Hall}
$\mu_0 H_{EB}$
I_{pulse} (mA)